Applied Catalysis B: Environmental 248 (2019) 22–30

Contents lists available at ScienceDirect

Applied Catalysis B: Environmental

journal homepage: www.elsevier.com/locate/apcatb

Nanospherical mesoporous carbon-supported gold as an efficient heterogeneous catalyst in the elimination of mass transport limitations

Shangjun Chen, Haibin Fu, Li Zhang, Ying Wan*

The Education Ministry Key Laboratory of Resource Chemistry, Shanghai Key Laboratory of Rare Earth Functional Materials, and Department of Chemistry, Shanghai Normal University, Shanghai 200234, PR China

ARTICLE INFO

Keywords:
Diffusion limitation
Nanosphere
Gold
Carbon
Selective hydrogenation

ABSTRACT

This study proposes ordered mesoporous carbon nanosphere-supported gold catalysts to eliminate the diffusion limitation inside the long channels of bulk mesoporous materials. The nanospherical catalysts have a spherical morphology with a diameter of approximately 90 nm, uniform pore sizes of 2.5 nm, and high surface areas of approximately 600 m^2/g; and the bulk catalysts have similar mesoporous textural properties with nanospherical catalysts but an irregular bulk shape. Metallic gold particles are both intercalated inside carbonaceous walls. The Madon-Boudart (MB) test shows that nanospherical catalysts exhibit no diffusion limitations in the reduction of nitroarenes, even for a large 2,6-dimethylnitrobenzene (2,6-DMNB) molecule. By comparison, the bulk-ordered mesoporous carbon-supported gold catalysts display distinct mass transfer inhibition. The nanospherical mesoporous carbon-supported gold catalysts are highly active and selective for the reduction of nitroarenes to corresponding amines, reaching turnover frequency (TOF) values of 13.7, 16.1, 7.6 and 26.8 min^{-1} for converting 4-nitrophenol (4-NP), 2-nitrophenol (2-NP), 4-(*tert*-butyl)-2-nitrophenol (4-TB-2-NP), and 2,6-DMNB, respectively. The catalysts are stable and can be re-used more than 15 times.

1. Introduction

Porous carbon is one of the most important materials for catalysts, adsorbents, sensors, and electrodes [1–4]. Carbon have many advantages compared with oxide supports, such as stability in both acidic and basic environments, electron conductivity, and a nearly limitless palette of properties, including tailoring porosity and surface chemistry [5,6]. Activated carbon with a disordered pore structure and a wide pore distribution is often used [7]. Ordered mesoporous materials with a uniform distribution of pores and a highly specific surface area are expected to exhibit several advantages over disordered materials when used as catalyst carriers and electrodes, such as metal particle size control, enhanced metal dispersion, and hindered active phase sintering [8,9].

Critically important for the application of mesoporous materials as adsorbents, electrodes and catalysts are the transport properties, particularly the intracrystalline diffusion [10]. The most widely employed ordered mesoporous materials, such as 2-dimensional (2D) hexagonal mesoporous silicate MCM-41, typically consist of large particles that are densely packed, are strictly parallel and lack interconnected mesopores, which result in a large diffusion length [11]. A more serious problem is pore blockage by metal or oxide nanoparticles upon loading catalytic active components, which may lead to a serious diffusion control process instead of a kinetic regime [12]. One of the characteristic properties of 2D hexagonal mesoporous silicate SBA-15, its 1D mesoporous network, could result in diffusion limitations upon reactants' arrival in industrial FT conditions [13]. By comparison, a short-channel RuCo/SBA-15 catalyst would lead to an enhanced selectivity toward the desired C5+ hydrocarbons due to a lower diffusional barrier between CO and the active sites. In addition, Lin and co-workers reported that Ru-containing mesoporous silicate nanospheres are highly active catalysts in the asymmetric hydrogenation of aromatic ketones, giving chiral secondary alcohols and racemic aryl aldehydes and thereby affording chiral primary alcohols [14]. Both the readily accessible and uniform catalytic sites within large mesochannels and the short diffusion length of mesoporous silicate nanospheres are considered to be of practical importance in asymmetric catalytic processes due to the typically large size (and hence hindered diffusion) of organic substrates. As a consequence, mesoporous carbon nanospheres (MCNs) have been fabricated to reduce mass transfer limitation in adsorption, catalysis, drug delivery, etc. both the hard-templating approach, using a pre-synthesized ordered mesoporous silica as a scaffold, and the soft-templating approach, using a block copolymer as a structure-directing agent, have been adopted [15,16]. Spherical ordered mesoporous carbon electrodes

* Corresponding author.
E-mail address: ywan@shnu.edu.cn (Y. Wan).

https://doi.org/10.1016/j.apcatb.2019.02.006
Received 21 September 2016; Received in revised form 28 June 2017; Accepted 4 February 2019
Available online 08 February 2019
0926-3373/

indeed show a better capacitance and capacitance retention than large-particle ones, possibly due to the small time constant, weak internal resistance and thus easy ion transport, particularly in an organic electrolyte [17]. But ordered mesoporous carbon nanospheres confined metal nanocatalysts, for example, gold nanocatalysts, have rarely been reported.

Gold nanocatalysts represent a new generation of catalysts for the selective oxidation of alcohols into the corresponding aldehydes, alkene, ketones, or carboxylic acid with molecular oxygen [18,19] and the selective reduction of nitroarenes into aminoarenes with hydrogen or sodium borohydride, with a significantly better selectivity and stability than platinum group metals [20–24]. Although several synthetic methods including deposition-precipitation (DP) and impregnation have been developed to load gold nanoparticles on oxide supports, such as CeO_2, TiO_2, ZrO_2, Fe_2O_3, etc. [25], immobilization of monodispersed Au nanoparticles on activated carbon remains a challenge. For example, under normal conditions in the DP process, $AuCl_4^-$ cannot be effectively deposited onto a negatively charged acidic carbon surface due to electronic repulsion. The impregnation method is also unfeasible, possibly due to the inert carbon matrix which show weak interaction with gold nanoparticles and therefore cannot anchor tiny particles with high surface energy [26]. The sol-gel preparation can be used to load gold on porous carbon [18,22,27]. The protecting agent for gold sols may influence the overall activity of gold catalysts in a variety of ways, such as by determining the particle size [28], the position of the Au nanoparticles (NPs) on the support surface, and the steric hindrance or electronic modification [29,30]. Upon the calcination of the protecting agent, particle growth at high temperatures, or even during reaction, accompanied by a loss of catalytic activity is a serious problem [31]. Additionally, the metal particles typically detach from the support in reuse, resulting in a sharp decrease in active sites [32]. Nanocasting is an alternative route to load gold on carbon, which includes the preparation of a gold-containing mesoporous silica hard template [33], the infiltration of carbon sources, and the carbonization and removal of silica scaffold [34,35]. Recently, our group reported a solvent evaporation-induced self-assembly using phenolic resin as the carbon source and $HAuCl_4$ as the gold source for the synthesis of a gold-containing mesoporous carbon catalyst [9]. The catalysts possess monodispersed gold nanoparticles, which intercalate into carbonaceous walls and uniform pore sizes, and show great advantages in terms of stability when converting benzyl alcohol into benzyl acid [36]. However, all efforts toward ordered mesoporous carbon-supported gold catalysts are limited in large carbon materials with a 2D hexagonal mesostructure. Gold nanoparticles are confined inside long 1D pore channels. In this context, mass transport limitations within a long pore length cannot be excluded, particularly for large molecules. Mesoporous carbon nanosphere-supported gold is therefore highly desired.

A one-step coordination-assisted hydrothermal synthesis in a dilute solution for the intercalation of monodispersed gold nanoparticles inside ordered mesoporous carbon nanospheres has been developed by our group. Ordered mesoporous carbon nanospheres (approximately 90 nm in diameter) intercalated with gold nanoparticles (approximately 2.8 nm in size) can be yielded. Here we highlight the elimination of the mass transport limitations due to the short diffusion path and mesopore sizes in nanospherical catalysts in reduction of nitroarenes to corresponding amines. In contrast, the “classically bulk” ordered mesoporous carbon-supported gold catalysts undergo serious mass transport limitations. The nanospherical gold catalysts are stable and can be reused with insignificant aggregation and leaching. These advantages pave the way for supported gold nanoparticles in practical applications, such as organic synthesis and sensors.

2. Experimental

2.1. Chemicals

Pluronic F127 (Mw = 12,600, $EO_{106}PO_{70}EO_{106}$), mercaptopropyltrimethoxysilane (MPTMS, minimum 98 wt%), tetraethyl orthosilicate (TEOS, minimum 99 wt%), 4-nitrophenol (4-NP, minimum 99 wt%), 2-nitrophenol (2-NP, minimum 99 wt%), 4-(*tert*-butyl)-2-nitrophenol (4-TB-2-NP, minimum 99 wt%), 2,6-dimethylnitrobenzene (2,6-DMNB, minimum 99 wt%) and thiourea (minimum 98 wt%) were purchased from Sigma-Aldrich Co. Chloroauric acid tetrahydrate ($HAuCl_4{\cdot}4H_2O$, Au minimum 47.8 wt%) and other chemicals were obtained from Sinopharm Group Co. Ltd. All the chemicals were used directly without further purification. Water used in all experiments was deionized.

2.2. Preparation of ordered mesoporous carbon supported gold nanocatalysts

Two procedures were applied here to synthesize ordered mesoporous carbon supported gold nanocatalysts, that is evaporation-induced self-assembly (EISA) for bulk catalysts (Au/OMC) [9,37] and hydrothermal synthesis for nanosphere catalysts (Au/MCN) [38].

1.0Au/MCN: A mixture composed of 0.6 g of phenol, 2.1 mL of formalin aqueous solution, and 15 mL of NaOH (0.1 mol/L) aqueous solution was firstly heated to 70 °C under stirring. After 30 min, a clear solution containing 1.2 g of Pluronic F127 and 15 g of deionized water was added to it. Then, the mixture was stirred at 66 °C for 3 h. The stirring speed was kept at 340 ± 40 rpm. Under stirring, a solution was further mixed with the above mixture, which was premade by mixing 0.128 g of MPTMS, 1.5 mL of $HAuCl_4$ aqueous solution (24.3 mmol/L) and 50 g of deionized water. Once the deposition appeared (normally it took 16–18 h), the reaction was immediately terminated. The deposition was re-dissolved upon quiescence. The solution was diluted. In general, 17.7 mL of the solution was diluted with 56 mL of H_2O. The diluted solution was transferred into several autoclaves. The hydrothermal treatment was adopted with 130 °C and 24 h. Then the autoclave was rapidly cooled to room temperature. After separation, washing with distilled water and drying at room temperature, the solid products were transferred to quartz boats and placed in a tubular furnace under protection of high purity nitrogen. The temperature program was from room temperature to 350 °C with a ramp of 1 °C/min, to 700 °C with 5 °C/min and maintenance at this temperature for 2 h, and cooling to room temperature. The final black powders were collected. Before use, the catalysts were treated at 150 °C for 4 h in air in an oven.

1.5Au/OMC: 3.2 g of Pluronic F127, 2.0 g of HCl (0.2 mol/L), 2.8 mL of $HAuCl_4$ solution (gold concentration in ethanol: 48.5 mmol/L), and 10.0 g of ethanol were mixed together under stirring at 40 °C. To it, a premade solution containing 2.08 g of TEOS, 1.97 g of MPTMS and 10.0 g of ethanol, and 10.0 g of phenolic resins ethanolic solution (20 wt%, Supplementary material) were added in sequence. The mixture was transferred to multiple dishes after 2 h-stirring. The dishes were placed in a hood to evaporate ethanol. The temperature was kept at 40 °C. Subsequently, they were placed into an oven to thermopolymerize resins. The temperature was kept at 100 °C and the time was kept for 24 h. After cooling to room temperature, the as-made light yellow films on the dishes were scratched and grounded into fine powders. The heating and post-treatment procedures are exactly the same as the nanospherical catalysts.

By tuning the $HAuCl_4$ amount, while maintaining the other parameters and processes of typical synthesis, the gold catalysts with various metal contents were obtained, denoted as xAu/MCN and xAu/OMC, where x represents the gold mass content determined by the ICP-AES analysis.

The benchmark samples include pristine MCN free of gold, and monodispersed gold nanoparticles stabilized with citrate. The synthesis procedures were provided in Supplementary material. The pristine

MCN has spherical morphology with a size of approximately 90 nm, the ordered cubic mesostructure, uniform mesopore diameter of 2.5 nm, a high BET surface of 650 m^2/g, and a large pore volume of 0.47 cm^3/g (Fig. S1). Gold nanoparticles stabilized with citrate have diameter of approximately 15 nm (Fig. S2).

2.3. Selective reduction of nitroarenes

First, 100 mL of aqueous $NaBH_4$ (176 mmol/L) solution was added to 3.5 mL of 4-NP (0.0193 mmol) solution with magnetic stirring of 800 rpm at 30 °C. Then, 20 mg of 1.0Au/MCN catalyst was added. At different time intervals, 3 mL of mixture was extracted by a syringe installed with a filtered membrane to separate solids, and the residue solution was immediately monitored with UV–vis spectra (Varian Cary 100). The kinetic study of the catalytic reaction was performed by plotting the change in the absorbance of 4-NP at 400 nm versus time. In a separated reaction, after the completion of the reaction, the reaction mixture was filtered, and the catalyst was washed thoroughly with ethanol. Then, the filtrate was concentrated and dried under reduced pressure using a rotary evaporator. The crude product was purified by column chromatography [silica 200–300; dichloromethane/petroleum ether mixture] to afford the product. The recovered material accounted for more than 95% of the starting material. All products were confirmed by ^1H NMR, and the spectra obtained were compared with the standard spectra. In some intervals, the conversion and yields were measured by high-performance liquid chromatography (HPLC, Agilent 1100 series) using a C18 reverse-phase column [ZORBAX Eclipse Plus C18 (4.6 × 100 mm)] and a diode array UV–vis detector. The estimation of conversion by the UV–vis spectra and HPLC corresponded well within an error of ± 5%. The reduction was repeated three times, yielding the same initial rates and total reaction times within ± 10%. The absorbance values, A_t and A_0, represent the absorption of 4-NP at concentrations of C_t and C_0, respectively, where t is the reaction time and C_0 is the initial concentration. The apparent rate constant (k_{app}) was calculated from the slope of the linear relationship between $\ln(C_t/C_0)$ and t. Catalytic results were also shown in terms of the conversion of nitroarenes: the turnover number (TON, total mmol of reacted nitroarenes *per* mmol of gold) and turnover frequency (TOF, molecules of converted nitroarene per surface atom of gold and minutes in the initial reaction period). Here, we followed the simplification by Rossi and co-workers, assuming in the model that both the total number of atoms and the related fraction of surface atoms, in a given gold particle, can be expressed as a continuous function of their diameter [39]. In a supported gold particle with a size of 2.8 nm, the surface atom/total atom ratio is calculated to be approximately 0.46, and the 9.0 nm particle exhibits a ratio of 0.17. Reactants with different molecular sizes were used, including 4-NP, 2-NP, 4-TB-2-NP, and 2,6-DMNB. The Newtonian ball and spring model, the molecular size, molecule weight and the wavelength for the UV absorption (water) for each reactant are listed in Table S1.

A hot infiltration test was conducted. The solid catalyst 1.0Au/MCN was filtered out of the reduction of 4-NP after 7 min, and the filtrate was monitored for continued activity [40]. A method reported by Jones and co-workers using mercapto-group modified mesoporous silica (SH-SBA-15) was used to trap soluble gold species [41]. In standard experiments, the two solids, i.e., SH-SBA-15 and supported gold catalysts with the molar ratio of SH:Au = 35:1, were mixed with an aqueous $NaBH_4$ solution for approximately 1 h. Then, the reaction was initiated by adding 4-NP solution. The SH-SBA-15 trapping agent is synthesized according to the well-established procedure of post-grafting and possesses accessible mercapto groups with a sulfur content of 2.5 mmol/g mesoporous silica, a 2D hexagonal mesostructure, a uniform pore size of 8.9 nm, a high surface area of 510 m^2/g, and a pore volume of 0.78 cm^3/g (Fig. S3).

For the thiourea poisoning experiment, a thiourea solution (2.0×10^{-4} to 1.02 mmol/L), prepared by dissolving the proper amount of thiourea in Milli-Q water, was added as the solvent while the other conditions were maintained the same.

The reduction of 4-NP was also performed using the recovered catalyst (maintaining the reaction conditions as the fresh one). After the reaction was completed, the 1.0Au/MCN catalyst was recovered by being thoroughly washed with a copious amount of ethanol and water, dried under vacuum at 80 °C overnight and weighed. Several parallel reactions were carried out to ensure that the catalyst amount was the same in each run. The gold content of the solid was measured at the first and last reuses. The aqueous solution after each cycle was collected to determine the gold leaching concentration.

2.4. Characterization

The morphology of nanospheres was observed by high-resolution scanning electron microscopy (HRSEM, JEOL S4800). TEM observations were performed using a JEM 2100 instrument operated at 200 kV. In order to better analyze the dispersion and the sizes of the gold nanoparticles, the samples were embedded in Spurr's resin and cut into ~ 50 nm thin sections using an ultramicrotome. The elemental analysis was conducted by energy-dispersive X-ray spectroscopy (EDX, Philips EDAX instrument). X-ray diffraction (XRD) measurements were taken on a Rigaku Dmax-3C diffractometer using Cu K_α radiation (40 kV, 20 mA, $\lambda = 0.15408$ nm). The metallic Au sizes were estimated according to the Scherrer formula, size = $0.89\lambda/\beta\cos\theta$, based on the 111 diffraction peaks in wide-angle XRD patterns. The small-angle X-ray scattering (SAXS) measurements were taken on a Nanostar U SAXS system (Bruker, Germany) using Cu Kα radiation (40 kV, 35 mA). The d-spacing values were calculated by the formula: $d = 2\pi / q$. N_2 adsorption- desorption isotherms were measured at 77 K with a Micromeritics TriStar II 3020 analyzer. The specific surface areas (S_{BET}) were calculated according to the Brunauer-Emmett-Teller (BET) method. The BET areas were reproducible to within ± 3%, and the values quoted in this study are the mean. The Barrett-Joyner-Halenda (BJH) model was used to calculate the pore volumes and pore size distributions. X-ray photoelectron spectroscopy (XPS) measurements were conducted on a Perkin-Elmer PHI 5000CESCA system with a monochromatic Mg K_α source and a charge neutralizer. Inductively coupled plasma-atomic emission spectrometry (ICP-AES, Varian VISTA-MPX) was used to determine the Au content. The silica component in the catalyst was etched by HF solution. After thoroughly washing and drying, the carbon support was burned in a crucible and the remaining metals could be dissolved in aqua regia [42]. The matrix of the calibration standards was adjusted to the matrix of the sample.

3. Results and discussion

3.1. Morphology, structure and textural properties of ordered mesoporous carbon supported gold catalysts

The SEM images show that the Au/MCN catalysts synthesized by hydrothermal treatment possess a spherical morphology, regardless of the gold content, similar to the literatures (in the experimental range of 0.5–1 wt%, Fig. S4) [38]. The nanospheres clearly display an ordered hexagonal array of mesopores on the exposed hemispheres in the HRSEM image for 1.0Au/MCN, indicative of an open pore structure on the surface (Fig. 1A). The mesopore diameters are estimated to be 2.5 nm. No aggregated gold nanoparticles larger than mesostructure domain size, with a lighter contract, can be found. The spherical morphology can also be clearly found in the TEM images for the thin slices of 1.0Au/MCN (Fig. 1B). The spheres have a diameter of approximately 90 nm, in good agreement with the SEM results. The typical images for the well-ordered body-centered cubic $Im\bar{3}m$ mesoporous structure, viewed along the [100], [110] and [111] directions can be observed in one image. Gold nanoparticles are highly dispersed, and locate inside the uniform mesopores, rather than stick on the sphere outer surface.

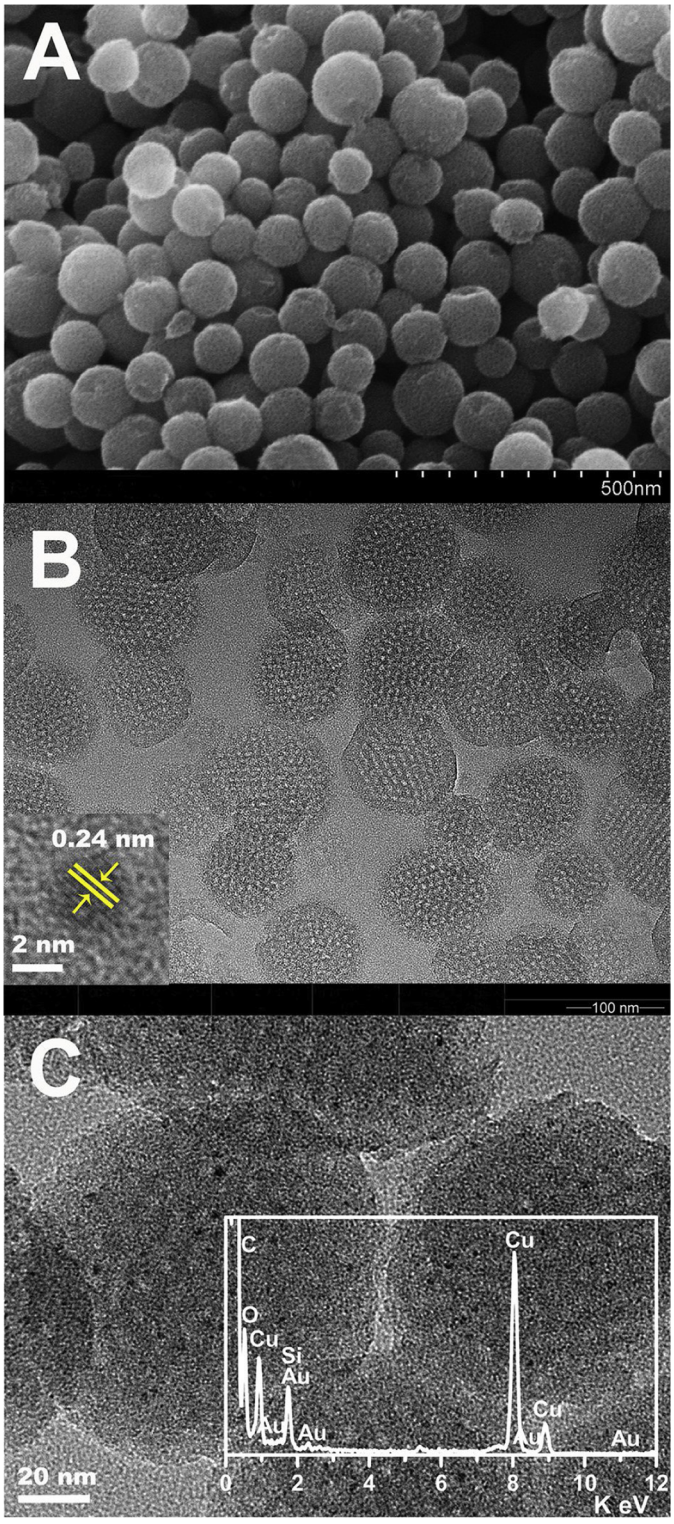

Fig. 1. (A) HRSEM and (B,C) TEM images for the nanospherical gold-containing ordered mesoporous carbon catalysts: (A,B) 1.0Au/MCN; (C) 0.8Au/MCN. (B) was taken from the thin slices. Inset B is the HRTEM image. Inset C is the EDX pattern.

The average gold nanoparticle size is approximately 2.8 nm (statistically the same as the other samples). The HRTEM image shows a representative particle, revealing the characteristic Au (111) lattice fringe at 0.24 nm. The gold content does not have a clear effect on the gold particle size, ordered cubic mesostructure and spherical morphology (Fig. 1C, Fig. S4). The EDX pattern reveals the presence of gold and the

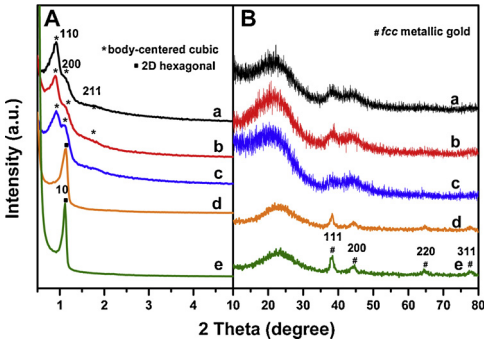

Fig. 2. (A) Small-angle and (B) wide-angle XRD patterns for nanospherical (Au/MCN) and bulk gold catalysts (Au/OMC) with different gold contents. (a) 1.0Au/MCN, (b) 0.8Au/MCN, (c) 0.5Au/MCN, (d) 1.5Au/OMC, and (e) 0.5Au/OMC.

absence of S. These phenomena indicate that the thermally stable gold nanoparticles are confined in the carbonaceous ordered mesostructure, and the elimination of sulfur upon high-temperature pyrolysis [38]. The resolved diffraction peaks in the small-angle range for Au/MCNs can be assigned to the 110, 200 and 211 reflections of a body-centered cubic $Im\bar{3}m$ mesostructured (Fig. 2). The cell parameter is estimated to be 13.3 nm. Broad diffractions at approximately 22° and 44° can be attributed to amorphous carbon. The additional diffused and broad diffraction at approximately 38° can be assigned to metallic gold, possibly due to the low content of gold with tiny particle sizes. These results are in consistent with the TEM images.

The HRSEM images for "classical bulk" powders of ordered mesoporous carbon-supported gold nanoparticles (Au/OMC) which were synthesized by a solvent evaporation-induced self-assembly approach, possess large particle sizes, i.e., in the micrometer range (Fig. 3). Hexagonally arranged pores are observed, suggesting open mesopores. But a much longer diffusion path compared to nanospheres can be drawn. The TEM images for both 0.5Au/OMC and 1.5Au/OMC show hexagonally arranged and straight-line pores in large domains, suggesting a 2D hexagonal mesostructure (Fig. S5). The gold particles uniformly distribute inside the particles without distinct aggregation to large particles. The particles are monodispersed with a size of approximately 9.0 nm, regardless of the gold content. Notably, the gold particles occupy both the pore space and pore walls. The well-resolved SAXRD patterns of the large-sized Au/OMC catalysts further confirms the 2D hexagonal mesostructure with 1D pore channels. The cell parameter (a_0) is calculated to be approximately 9.1 nm. The diffraction peaks in the wide-angle XRD patterns can be attributed to the *fcc* metallic gold. Estimation with the Scherrer formula gives rise to a gold particle size of approximately ~ 9.0 nm, regardless of the gold contents.

The XPS analysis is a surface sensitive technique with a sampling volume that extends from the surface to a depth of 1–5 nm [43]. The doublet with binding energies of approximately 88.0 and 84.3 eV in the XPS spectra for both 1.0Au/MCN and 1.5Au/OMC can be assigned to Au $4f_{7/2}$ and $4f_{5/2}$, respectively, in the metallic state (Fig. 4). The binding energy of S $2p_{3/2}$ in both samples nearly completely disappears, suggesting the depletion of S in the final gold catalysts (Fig. S6).

The Au/MCN spheres show a pseudo-type-IV nitrogen isotherms corresponding to a 3-D caged mesostructure with a narrow pore size distribution (Fig. 5). A hysteresis loop at a higher pressure (P/P_0 = 0.9-0.993) may reflect the interparticle texture between the carbon nanospheres. The most-probable pore sizes are calculated to be approximately 2.5 nm, in accordance with those measured from the TEM images (Table 1). The BET surface areas are calculated to be approximately 600 m^2/g, and the pore volumes are approximately 0.40 cm^3/g (Table 1). N_2 sorption isotherms for bulk-ordered mesoporous carbon-supported gold nanoparticles display typical type-IV isotherms

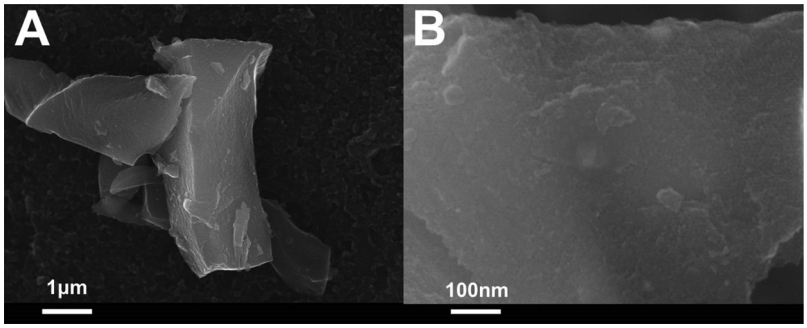

Fig. 3. Representative HRSEM images for bulk 1.5Au/OMC with (A) low and (B) high magnifications.

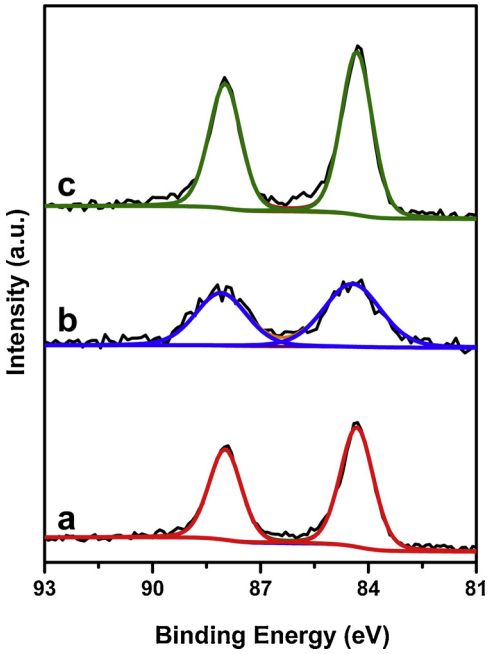

Fig. 4. XPS spectra in the Au *4f* region: (a) 1.0Au/MCN, (b) 1.0Au/MCN-R15 (1.0Au/MCN after 15 runs), and (c) 1.5Au/OMC.

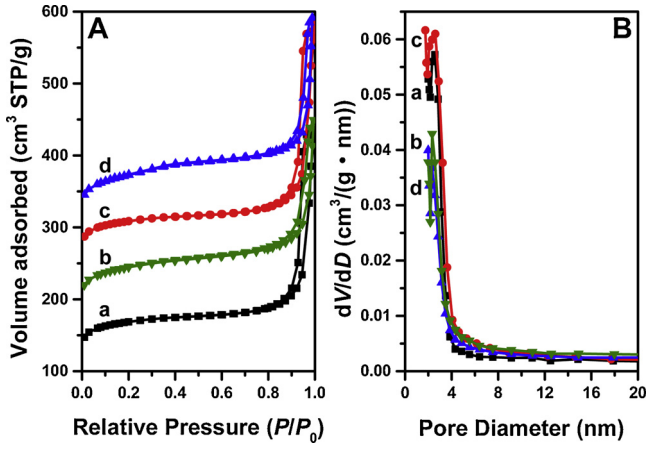

Fig. 5. (A) N_2 sorption isotherms and (B) pore size distribution curves for Au/MCN with different gold contents: (a) 0.5Au/MCN, (b) 0.8Au/MCN, (c) 1.0Au/MCN, and (d) re-used 1.0Au/MCN-R15. The curves in A are offset by 60, 120, and 180 cm^3 STP/g for b, c, and d, respectively.

characteristic of mesoporous solids with uniform pore sizes (Fig. S7). Narrow pore size distribution curves with a mean value of approximately 4.0 nm are calculated. The BET surface areas are approximately

Table 1
Structural and textual properties for gold-containing catalysts.

Sample	Au content[a] (wt%)	S_{BET} (m^2/g)	V_t (cm^3/g)	D_p (nm)	d_{Au}[b] (nm)	d_{Au}[c] (nm)
MCN	0	650	0.47	2.5	–	–
0.5Au/MCN	0.51	630	0.44	2.5	–	2.8
0.8Au/MCN	0.80	603	0.42	2.5	–	2.8
1.0Au/MCN	1.01	615	0.42	2.5	–	2.8
1.0Au/MCN-R15	1.01	620	0.41	2.5	–	2.8
0.5Au/OMC	0.54	450	0.33	4.3	9.1	9.0
1.5Au/OMC	1.51	418	0.32	4.2	9.2	9.0
Au sol	–	–	–	–	–	15

[a] Estimated by ICP-AES and TG analysis.
[b] Calculated from the Scherrer formula according to the 111 diffractions.
[c] Estimated from TEM analysis of average diameter.

400 m^2/g, and the pore volumes are 0.32 cm^3/g. The estimated pore-wall thickness is approximately 4.6 nm based on the hexagonal pore structure. The gold nanoparticle size in bulk Au/OMC is larger than either the pore size or wall thickness, further implying that gold particles occupy both the pore space and wall. H2-type hysteresis loops are observed. This phenomenon has also been observed in mesoporous carbon FDU-15 with a highly ordered 2D hexagonal mesostructured [44], which may have originated from the non-uniform pore surface of carbon materials and large mesopores partially blocked by gold nanoparticles [45]. The volume originated from micropores is as low as 0.05 cm^3/g for these catalysts. The lack of micropores hints that the large-sized powder Au/OMC catalysts have dense pore walls and few interconnected pores.

3.2. Selective reduction of nitroarenens with $NaBH_4$ over gold-containing catalysts

The reduction of nitroarenes with different molecular sizes, including 4-NP, 2-NP, 4-TB-2-NP, and 2,6-DMNB, by sodium borohydride were carried out to compare the activity among the carbon supported catalysts [46,47].The time-dependent UV–vis spectra for the reduction of 4-NP by $NaBH_4$ in the presence of 1.0Au/MCN display the simultaneous reduction in 4-NP absorbance at 400 nm, and the increase in 4-aminophenol absorbance (4-AP) at 300 nm over time (Fig. S8A). This phenomenon, together with the occurrence of isosbestic point at 315 nm, indicates that the reduction proceeds without producing byproducts. The absence of byproducts is also confirmed by ^1H NMR (Fig. S9). The product recovered after the completion of the reaction by column purification is solely indexed to the standard spectra of 4-AP. No other product is detected. The pseudo first-order reaction is considered because of the excess amount of $NaBH_4$. The k_{app} value, which is calculated from the slope of the linear relationship between $\ln(C_t/C_0)$ and the reaction time t, 0.34 min^{-1} from the slope, corresponding to a TOF value of 13.7 min^{-1} (Fig. 6, Table 2). Similar phenomena can be observed for the reduction of 2-NP to 2-AP, 4-TB-2-NP to 4-TB-2-AP,

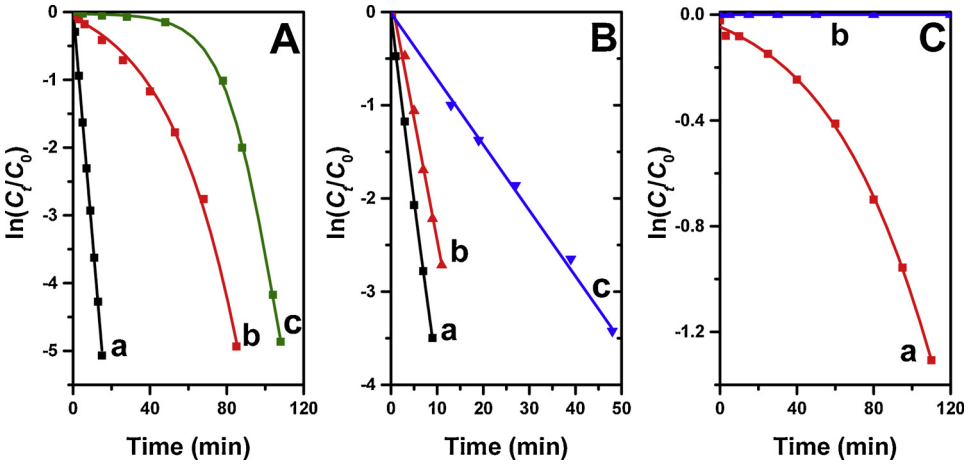

Fig. 6. Plot of $\ln(C_t/C_0)$ as a function of time (A) in the reduction of 4-NP over (a) 1.0Au/MCN, (b) gold on large-sized ordered mesoporous carbon 1.5Au/OMC and (c) 0.5Au/OMC; (B) in the reduction of (a) 2-NP, (b) 4-TB-2-NP, (c) 2,6-DMNB over 1.0Au/MCN; and (C) in the reduction of 2,6-DMNB over (a) 1.5Au/OMC, and (b) bulk 0.5Au/OMC. Reaction conditions: 20 mg of catalyst, 0.0193 mmol of 4-NP, 0.0193 mmol 2-NP, 0.0137 mmol 4-TB-2-NP, or 0.178 mmol 2,6-DMNB; 17.6 mmol of $NaBH_4$; 100 mL of water (solvent); 30 °C.

Table 2
Catalytic performance for the nitroarenes reduction over gold-containing catalysts.

Sample	Substrate	C_0 (mol)	n_{Au} (mol)	k_{app} (min^{-1})	k_{aAu} (min^{-1} $mmol^{-1}$)	r_0 (min^{-1})	TOF (min^{-1})
1.0Au/MCN	4-NP	1.93×10^{-5}	1.02×10^{-6}	0.34	328	6.3	13.7
	2-NP	1.93×10^{-5}	1.02×10^{-6}	0.39	382	7.4	16.1
	4-TB-2-NP	1.37×10^{-5}	1.02×10^{-6}	0.26	256	3.5	7.6
	2,6-DMNB	1.78×10^{-4}	1.02×10^{-6}	0.071	70	12.4	26.8
0.8Au/MCN	4-NP	1.93×10^{-5}	1.02×10^{-6}	0.32	314	6.1	13.3
	4-NP	1.93×10^{-5}	0.81×10^{-6}	0.25	309	6.0	13.0
	2,6-DMNB	1.78×10^{-4}	1.02×10^{-6}	0.068	67	11.6	25.2
	2,6-DMNB	1.78×10^{-4}	0.81×10^{-6}	0.054	67	11.9	25.9
0.5Au/MCN	4-NP	1.93×10^{-5}	1.02×10^{-6}	0.31	304	5.9	12.8
	4-NP	1.93×10^{-5}	0.52×10^{-6}	0.158	304	5.9	12.8
	2,6-DMNB	1.78×10^{-4}	1.02×10^{-6}	0.072	71	12.6	27.4
	2,6-DMNB	1.78×10^{-4}	0.52×10^{-6}	0.037	70	12.5	27.2
Au sol	4-NP	1.93×10^{-5}	0.38×10^{-6}	0.46	1210	23.4	292.5

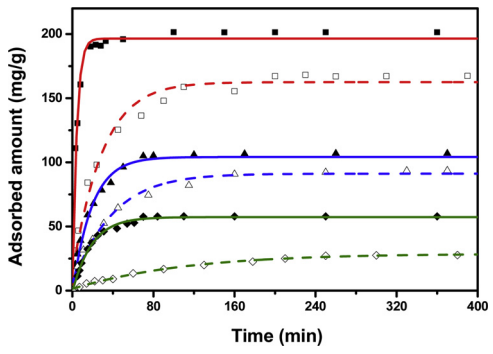

Fig. 7. Adsorption capacities with various concentrations on spherical 1.0Au/MCN (solid line) and large-sized 0.5Au/OMC (dash line) catalysts as a function of the contacting time: 4-NP (400 mg/L) in the absence of $NaBH_4$ (red line, square); 4-NP (26.8 mg/L) in the absence of $NaBH_4$ (blue line, triangle); and on MCN (solid line) and large-sized OMC (dash line) for 4-NP (26.8 mg/L) in the presence of $NaBH_4$ (reaction condition, green line, diamonde) (For interpretation of the references to colour in this figure legend, the reader is referred to the web version of this article).

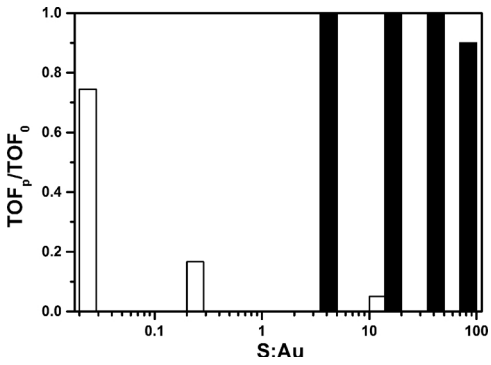

Fig. 8. Residual activity after addition of various amounts of thiourea for selective reduction of 4-NP over soluble gold nanoparticles stabilized by citrate (open column) and nanospherical gold-intercalated ordered mesoporous carbon catalyst (solid column). Reaction conditions: 20 mg of 1.0Au/MCN (n_{Au} of 0.00102 mmol) or 1.5 mL of gold nanoparticles stabilized by citrate (n_{Au} of 0.00038 mmol), 0.0193 mmol of 4-NP; 17.6 mmol of $NaBH_4$; 100 mL of aqueous thiourea solution containing 0.02 μmol – 0.102 mmol of thiourea; 30 °C; and 800 rpm.

and 2,6-DMNB to 2,6-DMAB, i.e., an undetectable byproduct analyzed by ^1H NMR and a pseudo first-order reaction kinetics curve (Fig. S8B-D, Fig. S9). The TOF values are calculated to be 16.1, 7.6, and 26.8 min^{-1} for the reduction of 2-NP, 4-TB-2-NP, and 2,6-DMNB, respectively, and comparable to the reported gold nanocatalysts and transition-metal containing catalysts (Table S2) [48–52].

In the absence of $NaBH_4$, a decrease in 4-NP (26.8 mg/L) is detected with an equilibrium adsorption amount (Q_e) of 0.75 mmol/g within 70 min (Fig. S10, Fig. 7); 4-AP is under-detected. The pristine MCN without gold also displays adsorption under the reaction conditions, indicating that the thermodynamically favorable reduction of the nitro compounds (E_0 for 4-NP/4-AP = -0.76 V and H_3BO_3/BH_4^- = 1.33 V, *versus* NHE) is not observed in the absence of gold nanoparticles [53]. The Q_e value reduces to 0.38 mmol/g. The pristine MCN has similar

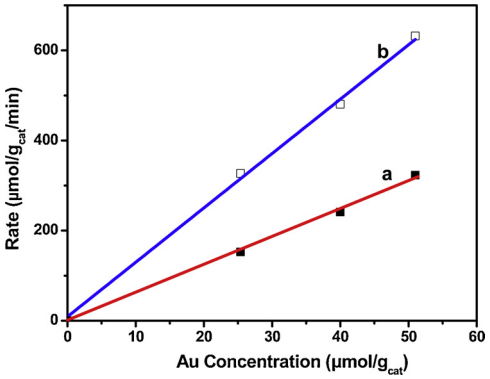

Fig. 9. Effect of Au loading (the Madon-Boudart test) on the reaction rate of the selective reduction of (a) 4-NP (■, red line) and (b) 2,6-DMNB (□, blue line) using the nanospherical *x*Au/MCN catalysts. Reaction conditions: 20 mg of catalyst (Au loading of 0.51 wt%, 0.80 wt% and 1.01 wt%, respectively), 0.0193 mmol of 4-NP or 0.178 mmol of 2,6-DMNB; 17.6 mmol of $NaBH_4$; 100 mL of water (solvent); 30 °C; and 800 rpm. (For interpretation of the references to colour in this figure legend, the reader is referred to the web version of this article).

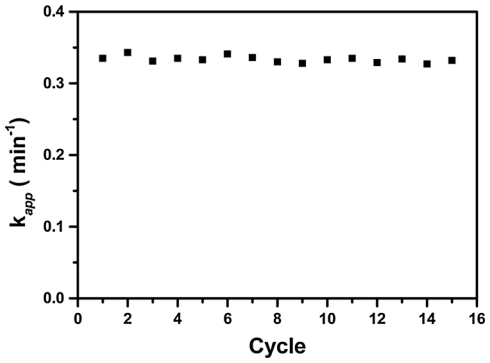

Fig. 10. Apparent rate constant for the catalytic conversion of 4-NP in successive runs over the recovered 1.0Au/MCN catalyst.

morphology, textural and structural properties as 1.0Au/MCN, the difference in Q_e for 4-NP is highly related to the presence of a large amount of $NaBH_4$ in the solution. The 4-NP aqueous solution shows an absorption maximum at 317 nm due to the n → π* transition. This peak is red shifted to 400 nm immediately after the addition of $NaBH_4$ due to the formation of 4-nitrophenolate ions in alkaline solution [54]. The adsorption of the coordination ion is inhibited inside carbon mesopores. These results demonstrate the adsorption of the reactant inside mesopores, and the accessible gold nanoparticles in the MCN matrix catalyze the selective reduction.

The reduction of 4-NP over bulk 0.5Au/OMC undergoes two processes: a slow decrease in concentration in the initial period (60 min), similarly to the adsorption of a gold-free sample (OMC, Fig. S10C), and then a rapid reduction. This phenomenon is different with most gold nanoparticle catalysts [51,55]. The 0.5Au/OMC catalyst is then re-used and behaves similarly, i.e., an adsorption followed by a catalytic reduction (Fig. S11).

The hot filtration test is considered a strong test for assessing the presence of soluble active metallic species. In this procedure, solid catalysts are filtered out of the reaction, and the filtrate is monitored for continued activity [40]. When 1.0Au/MCN is hot filtered during reaction with an incomplete conversion, the filtrate loses its activity, which demonstrates a heterogeneous catalysis (Fig. S12). The addition of solid trapping agent SH-SBA-15 to the reaction batches exhibits a slight change for the conversion plots for both 1.0Au/MCN and bulk 1.5Au/OMC, demonstrating the heterogeneous catalysis by nanoparticles inside the matrix (Fig. S13).

3.3. Elimination of mass transfer

The external mass transfer limitations are avoided by stirring at 800 rpm. The Madon-Boudart (MB) test is further used to verify the mass transfer effects during the selective reduction of nitroarenes, which requires the measurement of the reaction rate (on *per* μmol metal basis) for catalysts with varying surface concentrations of metal but with similar dispersion [56]. As described in 3.1, the nanospherical Au/MCN and bulk Au/OMC catalysts with different metal loadings show similar metal dispersions.

The k_{app} values for the reduction of 4-NP decreases with decrease in the gold contents from 0.51 wt% to 1.01 wt% of the spherical Au/MCN. A plot of the reduction rate versus surface concentration over the nanospherical catalysts yields a straight line (Fig. 9). Similar result has been observed for the reduction of a large-molecule substrate of 2,6-DMNB with *n*(Au): *n*(2,6-DMNB) ranging from 1:342 to 1:174, demonstrating that the mass transfer effect is absent.

Both 0.5Au/OMC and 1.5Au/OMC with gold loading of 0.54 wt% and 1.51 wt%, respectively, behave two-step process in the reduction of 4-NP, possibly due to the mass diffusion limitation. The initial slow process is clearly accelerated with an increase in gold loading, implying the improvement in the reduction over accessible gold nanoparticles in 1.5Au/OMC. When using 2,6-DMNB as the substrate, the 0.5Au/OMC catalyst does not show a clear reduction within 2 h even with a *n*(Au): *n* (2,6-DMNB) ratio of 162, indicating the serious diffusion limitations for the large-sized molecules (Fig. 6C). Gold nanoparticles in the long tunnels are inaccessible. An increase in the gold concentration leads to the occurrence of catalysis, implying the enhanced accessibility of gold nanoparticles. However, the pseudo first-order reaction kinetics curve can also not be obtained.

We have previously shown that the intrinsic activity at 25 °C is nearly independent of size (in the range from 3.0 to 9.0 nm) for gold on carbon catalysts [36]. Because the nanospherical and bulk catalysts have similar BET surface areas, the large difference may be related to the mass transfer inside mesopores and thus the accessibility of gold-active sites. Diffusion restriction is distinct for large-powdered ordered mesoporous carbon-supported gold catalysts in the reduction of

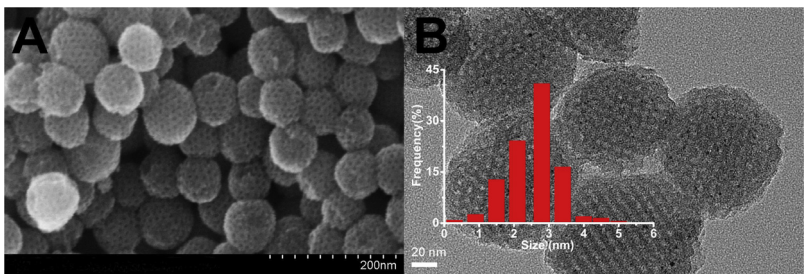

Fig. 11. (A) HRSEM and (B) TEM images for the 1.0Au/MCN-R15 catalyst after 15 catalytic runs for reduction of 4-nitrophenol by $NaBH_4$. Inset B is the gold particle size distribution histogram.

nitroarenes, particularly for the catalyst with a low gold loading. These catalysts possess dense pore walls with local uniformity and ordered 1D channel arrays, and they lack interconnected micropores, similar to mesoporous silicate MCM-41.

The adsorption isotherms of 4-NP are further investigated over gold-containing mesoporous carbon catalysts with various morphologies (Fig. 7). The curve for the adsorption capacity of 4-NP (400 mg/L) over 1.0Au/MCN as a function of the contacting time displays a predominant increase in the initial period with rapid adsorption, and the saturated adsorption can be reached within 15 min, indicating extremely rapid adsorption. When the initial concentration decreases to 26.8 mg/L (reaction conditions), it takes approximately 45 min for adsorption equilibrium to be reached, after which the adsorption rate decreases. As mentioned above, the adsorption for 4-NP is further restricted to some extent in the presence of $NaBH_4$ in MCN. By comparison, large-sized 0.5Au/OMC possesses a slightly lower equilibrium adsorption amount but with a slower propagation rate for 4-NP compared to the spherical catalyst. The restriction is much serious in the presence of $NaBH_4$ for large-sized OMC. The initial adsorption rate decreases by almost 3-fold compared to MCN.

The time constant for diffusion inside pores is proportional to effective diffusivity and inversely related to the square of the pore length [57]. In fact, the effective diffusivity is highly dependent on the porosity (determined by pore size and volume) and tortuosity (determined by pore length and shape) of the support material [58]. For example, in mesoporous silicate MCM-41, the major diffusion, which represents diffusivity in the direction of the axis of symmetry, is attributed to diffusion in the direction of the channels of the MCM-41 structure. It is slower than in the free liquid by approximately one order of magnitude, which is clearly inhibited by a partial channel blockage [59]. Simultaneously, although it is considerably smaller than the diffusivity in the axis direction, there is also a finite of molecular propagation perpendicular to the channel axes [58,60]. Thus, the channel walls should be considered somewhat permeable to water molecules due to the surface hydroxyl groups [59]. However, the permeation to the organic substrate molecules maybe restricted. Therefore, the diffusion along the 1D channels in the large-sized powdered Au/OMC catalysts may be predominant. The long pore channels and pore blockage by gold nanoparticles is possible reasons for the slow propagation rate of guest molecules in micron-sized mesoporous carbons. The inaccessibility to the low-concentration gold nanoparticles that are encapsulated inside long channels leads to the “dominance” of the catalyst in the first 30 min over the 0.5Au/OMC for 4-NP reduction. Once the substrate molecules reach the gold surface, the reduction occurs. As such, the diffusion limitation is predominant for a large-molecule reduction, such as 2,6-DMNB. The reduction is not notable within 2 h. When the gold loading increases to 1.51 wt%, partial gold nanoparticles are easily accessible. The catalytic reduction, even for 2,6-DMNB, can occur. However, the diffusion limitation is still serious because the pseudo first-order kinetics cannot be obtained. It should be mentioned here that the steric effect may also play a significant role for the possibility of hydrogenation of 2,6-DMNB.

In contrast, nanospherical catalysts exhibit a negligible mass transfer effect. The predominant increase in the guest molecules in pores in the initial period and a rapid adsorption equilibrium suggest rapid diffusion. These phenomena demonstrate the elimination of diffusion limitations in micron-sized catalysts with a long diffusion channel by nanospheres with a short diffusion path. All gold nanoparticles can be easily reached by substrates. Thus, an intrinsic kinetics regime is obtained, and this type of catalyst can serve as the model catalysts for further investigation.

3.4. Poisoning-resistance intercalated gold nanocatalysts

Thiourea may be able to tune the electronic properties of Au *via* electron resonance from the ligand to the metal center [61]. The introduction of thiourea to the Au/C-catalyzed aerobic oxidation of glucose in water would almost completely quench the reaction with a S:Au molar ratio as low as 0.05 [61]. Fig. 8 displays the normalized conversions of the reaction as a functional of the concentrations of thiourea. Note that the concentrations of thiourea are shown relative to the total number of Au atoms. Monodispersed gold nanoparticles exhibit a rapid reduction of 4-NP with a TOF value of 292.5 min^{-1}, nearly 21 times higher than that of 1.0Au/MCN [38]. However, the gold sols stabilized by citrate undergo a serious poisoning by thiourea at a low concentration in 4-NP reduction. A dramatic decrease by approximately 85% is detected in the presence of 2.04×10^{-4} mmol of thiourea (S:Au of 0.2 in molar ratio). A complete quench occurs with S:Au of 50. On contrast, negligible decrease can be observed over 1.0Au/MCN even with an exposure to thiourea with S:Au of 50 in the reduction of 4-NP. Approximately 89% activity can be retained when S:Au reaches 100. This phenomenon indicates that intercalated gold nanoparticles are possibly inaccessible to thiourea in hydrogenation, and the leaching gold nanoparticles from 1.0Au/MCN can be almost ruled out.

The competitive adsorption of substrate over poison could improve the poisoning inaccessibility to active centers [62]. On one hand, soluble thiourea may majorly remains in water solution instead of adsorbs inside the pores due to the hydrophobicity of carbon support. On the other hand, the coordination between 4-nitrophenolate ions and BH_4^- can be strongly adsorbed on the gold surface inside the pores, and further reduced to aminophenol. The presence of an excess of BH_4^- may resist the adsorption of thiourea on gold surface. The poisoning mechanism is deserved to be separately reported regarding various sulfur-containing molecules.

3.5. Reusability of Au/MCN nanospheres

The k_{app} values for the catalytic conversion of 4-NP over the recovered 1.0Au/MCN catalysts are similar to those obtained over the fresh catalyst (Fig. S14); the compiled data in successive runs are shown in Fig. 10. No clear changes are detected in the catalytic performance after 15 runs, demonstrating that the reused catalyst maintains the reaction rate and conversion. The reaction mother liquors after separation of the catalyst in each run were collected and mixed. The gold content in the final mixture is below the detection limit of ICP-AES analysis, implying that negligible metal leaching occurs during repeated reactions on the same catalyst. These results suggest that the nanospherical carbon-supported gold catalyst is stable and reusable.

Characterization of the reused catalyst further confirms the stability of the nanospherical mesoporous carbon-supported gold catalyst during the reaction. The metallic gold in the carbon framework can be maintained as evidenced by the XPS spectrum of 1.0Au/MCN-R15, which is similar to the fresh catalyst (Fig. 4). The TEM images for the reused catalyst show similar spherical morphology as the diameter of approximately 90 nm, the cubic mesostructure, and monodispersed gold nanoparticles with a size of 2.8 nm inside the matrix, indicating the well stability of the catalyst (Fig. 11). Compared with the fresh catalyst 1.0Au/MCN, the N_2 sorption isotherms of 1.0Au/MCN-R15 after 15 successive runs exhibit only slight changes in the structural and textual properties, which indicate that the high surface area and uniform mesopores of the catalyst can be well retained (Fig. 5).

4. Conclusions

Nanospherical ordered mesoporous carbon-supported gold catalysts are synthesized to eliminate the diffusion limitation inside the long channels of bulk mesoporous materials. Gold nanoparticles in nanospheres are fully accessible by substrate due to the open mesopores and short diffusion path. This type of catalyst is highly active and selective and free of diffusion limitations in the selective reduction of nitroarenes. In contrast, the classical bulk-ordered mesoporous carbon-supported gold catalysts display distinct mass transfer inhibition,

particularly in large-molecule involved reactions. The nanospherical gold catalysts are stable and reusable.

Acknowledgements

This work was supported by the State Key Basic Research Program of China (2013CB934102), the NSF of China (21322308), the Ministry of Education of China (PCSIRT-IRT1269), and the Shanghai Sci. & Tech. and Edu. Committee (11JC1409200).

Appendix A. Supplementary data

Supplementary material related to this article can be found, in the online version, at doi:https://doi.org/10.1016/j.apcatb.2019.02.006.

References

[1] C. Liang, Z. Li, S. Dai, Angew. Chem. Int. Ed. 47 (2008) 3696–3717.
[2] J. Liu, N.P. Wickramaratne, S.Z. Qiao, M. Jaroniec, Nat. Mater. 14 (2015) 763–774.
[3] Q. Wang, J. Yan, Z.J. Fan, Energy Environ. Sci. 9 (2016) 729–762.
[4] T.Y. Ma, L. Liu, Z.Y. Yuan, Chem. Soc. Rev. 42 (2013) 3977–4003.
[5] L. Prati, A. Villa, A.R. Lupini, G.M. Veith, Phys. Chem. Chem. Phys. 14 (2012) 2969–2978.
[6] J. Matthiesen, T. Hoff, C. Liu, C. Pueschel, R. Rao, J.-P. Tessonnier, Chin. J. Catal. 35 (2014) 842–855.
[7] H. Marsh, F. Rodríguez-Reinoso, Activated Carbon, Elsevier, Amsterdam, London, 2006.
[8] A. Vu, X.Y. Li, J. Phillips, A.J. Han, W.H. Smyrl, P. Buhlmann, A. Stein, Chem. Mater. 25 (2013) 4137–4148.
[9] S. Wang, Q. Zhao, H. Wei, J.-Q. Wang, M. Cho, H.S. Cho, O. Terasaki, Y. Wan, J. Am. Chem. Soc. 135 (2013) 11849–11860.
[10] J. Karger, R. Valiullin, Chem. Soc. Rev. 42 (2013) 4172–4197.
[11] Z. Adem, F. Guenneau, M.A. Springuel-Huet, A. Gedeon, J. Iapichella, T. Cacciaguerra, A. Galarneau, J. Phys. Chem. C 116 (2012) 13749–13759.
[12] R. Li, J.A. Fowler, B.A. Todd, Phys. Rev. Lett. 113 (2014) 028303.
[13] G. Prieto, A. Martínez, R. Murciano, M.A. Arribas, Appl. Catal. A Gen. 367 (2009) 146–156.
[14] D.J. Mihalcik, W. Lin, Angew. Chem. Int. Ed. 47 (2008) 6229–6232.
[15] A.B. Fuertes, J. Mater. Chem. 13 (2003) 3085–3088.
[16] Y. Fang, Y. Lv, F. Gong, Z. Wu, X. Li, H. Zhu, L. Zhou, C. Yao, F. Zhang, G. Zheng, D. Zhao, J. Am. Chem. Soc. 137 (2015) 2808–2811.
[17] X. Yu, J.-g. Wang, Z.-H. Huang, W. Shen, F. Kang, Electrochem. Commun. 36 (2013) 66–70.
[18] L. Prati, M. Rossi, J. Catal. 176 (1998) 552–560.
[19] H. Wang, Y. Shi, M. Haruta, J. Huang, Appl. Catal. A 536 (2017) 27–34.
[20] A. Corma, A. Leyva-Perez, M.J. Sabater, Chem. Rev. 111 (2011) 1657–1712.
[21] R.-Y. Zhong, K.-Q. Sun, Y.-C. Hong, B.-Q. Xu, ACS Catal. 4 (2014) 3982–3993.
[22] A. Corma, H. Garcia, Chem. Soc. Rev. 37 (2008) 2096–2126.
[23] A. Villa, N. Dimitratos, C.E. Chan-Thaw, C. Hammond, G.M. Veith, D. Wang, M. Manzoli, L. Prati, G.J. Hutchings, Chem. Soc. Rev. 45 (2016) 4953–4994.
[24] L. Yu, Q. Zhang, S.-S. Li, J. Huang, Y.-M. Liu, H.-Y. He, Y. Cao, ChemSusChem 8 (2015) 3029–3035.
[25] T. Akita, M. Kohyama, M. Haruta, Acc. Chem. Res. 46 (2013) 1773–1782.
[26] J. Sá, A. Goguet, S.F.R. Taylor, R. Tiruvalam, C.J. Kiely, M. Nachtegaal, G.J. Hutchings, C. Hardacre, Angew. Chem. Int. Ed. 50 (2011) 8912–8916.
[27] A. Villa, N. Janjic, P. Spontoni, D. Wang, D.S. Su, L. Prati, Appl. Catal. A Gen. 364 (2009) 221–228.
[28] N. Dimitratos, J. Lopez-Sanchez, D. Lennon, F. Porta, L. Prati, A. Villa, Catal. Lett. 108 (2006) 147–153.
[29] A. Villa, D. Wang, D. Su, G.M. Veith, L. Prati, Phys. Chem. Chem. Phys. 12 (2010) 2183–2189.
[30] R.-Y. Zhong, X.-H. Yan, Z.-K. Gao, R.-J. Zhang, B.-Q. Xu, Catal. Sci. Technol. 3 (2013) 3013–3019.
[31] T.W. Hansen, A.T. DeLaRiva, S.R. Challa, A.K. Datye, Acc. Chem. Res. 46 (2013) 1720–1730.
[32] Y. Wang, S. Van de Vyver, K.K. Sharma, Y. Roman-Leshkov, Green Chem. 16 (2014) 719–726.
[33] P. Wu, P. Bai, Z. Lei, K.P. Loh, X.S. Zhao, Microporous Mesoporous Mater. 141 (2011) 222–230.
[34] F. Kerdi, V. Caps, A. Tuel, Microporous Mesoporous Mater. 140 (2011) 89–96.
[35] Z. Ma, S. Dai, ACS Catal. 1 (2011) 805–818.
[36] S. Wang, J. Wang, Q. Zhao, D. Li, J.-Q. Wang, M. Cho, H. Cho, O. Terasaki, S. Chen, Y. Wan, ACS Catal. 5 (2015) 797–802.
[37] S. Wang, J. Wang, X. Zhu, J. Wang, O. Terasaki, Y. Wan, Chin. J. Catal. 37 (2016) 61–72.
[38] H. Fu, L. Zhang, Y. Wang, S. Chen, Y. Wan, J. Catal. 344 (2016) 313–324.
[39] M. Comotti, C. Della Pina, R. Matarrese, M. Rossi, Angew. Chem. Int. Ed. 43 (2004) 5812–5815.
[40] R.A. Sheldon, M. Wallau, I.W.C.E. Arends, U. Schuchardt, Acc. Chem. Res. 31 (1998) 485–493.
[41] J.M. Richardson, C.W. Jones, J. Catal. 251 (2007) 80–93.
[42] S. Marx, A. Baiker, J. Phys. Chem. C 113 (2009) 6191–6201.
[43] S. Tougaard, Surf. Interface Anal. 26 (1998) 249–269.
[44] Y. Meng, D. Gu, F. Zhang, Y. Shi, H. Yang, Z. Li, C. Yu, B. Tu, D. Zhao, Angew. Chem. Int. Ed. 44 (2005) 7053–7059.
[45] K.K.R. Datta, B.V.S. Reddy, K. Ariga, A. Vinu, Angew. Chem. Int. Ed. 49 (2010) 5961–5965.
[46] J. Guo, K.S. Suslick, Chem. Commun. 48 (2012) 11094–11096.
[47] P. Veerakumar, I. Panneer Muthuselvam, C.-T. Hung, K.-C. Lin, F.-C. Chou, S.-B. Liu, ACS Sustain. Chem. Eng. 4 (2016) 6772–6782.
[48] S. Fountoulaki, V. Daikopoulou, P.L. Gkizis, I. Tamiolakis, G.S. Armatas, I.N. Lykakis, ACS Catal. 4 (2014) 3504–3511.
[49] B. Kaur, M. Tumma, R. Srivastava, Ind. Eng. Chem. Res. 52 (2013) 11479–11487.
[50] M. Tumma, R. Srivastava, Catal. Commun. 37 (2013) 64–68.
[51] S.-H. Wu, C.-T. Tseng, Y.-S. Lin, C.-H. Lin, Y. Hung, C.-Y. Mou, J. Mater. Chem. 21 (2011) 789–794.
[52] S. Wang, M. Zhang, W. Zhang, ACS Catal. 1 (2011) 207–211.
[53] S. Jana, S.K. Ghosh, S. Nath, S. Pande, S. Praharaj, S. Panigrahi, S. Basu, T. Endo, T. Pal, Appl. Catal. A Gen. 313 (2006) 41–48.
[54] T. Aditya, A. Pal, T. Pal, Chem. Commun. 51 (2015) 9410–9431.
[55] X. Fang, J. Zang, X. Wang, M.-S. Zheng, N. Zheng, J. Mater. Chem. A (2014) 6191–6197.
[56] R.J. Madon, M. Boudart, Ind. Eng. Chem. Fundam. 21 (1982) 438–447.
[57] J. Kärger, D. Ruthven, Diffusion in Zeolites and Other Microporous Materials, John Wiley and Sons, New York, 1992.
[58] H. Alsyouri, O.C. Gobin, A. Jentys, J.A. Lercher, J. Phys. Chem. C 115 (2011) 8602–8612.
[59] F. Stallmach, J. Kärger, C. Krause, M. Jeschke, U. Oberhagemann, J. Am. Chem. Soc. 122 (2000) 9237–9242.
[60] J.C. Groen, W. Zhu, S. Brouwer, S.J. Huynink, F. Kapteijn, J.A. Moulijn, J. Pérez-Ramírez, J. Am. Chem. Soc. 129 (2007) 355–360.
[61] C. Della Pina, E. Falletta, M. Rossi, A. Sacco, J. Catal. 263 (2009) 92–97.
[62] P. Haider, A. Urakawa, E. Schmidt, A. Baiker, J. Mol. Catal. A Chem. 305 (2009) 161–169.